JOURNAL OF SYNCHROTRON RADIATION
ISSN 1600-5775

Probing disorder in high-pressure cubic tin (IV) oxide: a combined X-ray diffraction and absorption study

Daniel Sneed,[a]* John S. C. Kearney,[a] Dean Smith,[a] Jesse S. Smith,[b] Changyong Park[b] and Ashkan Salamat[a]*

[a]Department of Physics and Astronomy, and HiPSEC, University of Nevada Las Vegas, Las Vegas, NV 89154, USA, and [b]HPCAT, X-ray Science Division, Argonne National Laboratory, Argonne, IL 60439, USA.
*Correspondence e-mail: sneedd3@unlv.nevada.edu, salamat@physics.unlv.edu

Received 5 February 2019
Accepted 21 March 2019

Edited by I. Lindau, SLAC/Stanford University, USA

Keywords: extreme conditions; EXAFS; XRD; laser heating; SnO_2; diamond anvil cell; high pressure.

The transparent conducting oxide, SnO_2, is a promising optoelectronic material with predicted tailorable properties *via* pressure-mediated band gap opening. While such electronic properties are typically modeled assuming perfect crystallinity, disordering of the O sublattice under pressure is qualitatively known. Here a quantitative approach is thus employed, combining extended X-ray absorption fine-structure (EXAFS) spectroscopy with X-ray diffraction, to probe the extent of Sn—O bond anharmonicities in the high-pressure cubic ($Pa\bar{3}$) SnO_2 – formed as a single phase and annealed by CO_2 laser heating to 2648 ± 41 K at 44.5 GPa. This combinational study reveals and quantifies a large degree of disordering in the O sublattice, while the Sn lattice remains ordered. Moreover, this study describes implementation of direct laser heating of non-metallic samples by CO_2 laser alongside EXAFS, and the high quality of data which may be achieved at high pressures in a diamond anvil cell when appropriate thermal annealing is applied.

1. Introduction

The intrinsic link between the structure of a material and its physical properties demands the most accurate determination of atomic configuration. The Z^2 scaling of atomic scattering power in X-ray diffraction (XRD) causes heavier elements to dominate signals, reducing its effectiveness for probing lighter species in compounds. Meanwhile, X-ray absorption spectroscopy (XAS) provides a probe for determining bond orders and local environments of a specific atom. Extended X-ray absorption fine-structure (EXAFS) spectroscopy directly probes interatomic distances and geometries with a $1/R^2$ dependence.

There are now numerous instruments at large-scale facilities dedicated to XAS at extreme conditions. High-brilliance sources and X-ray micro-focusing enable measurements within the confines of a diamond anvil cell (DAC) and laser-heated DAC for static high-pressure measurements, and these instruments are now beginning to access dynamic regimes (Aquilanti *et al.*, 2003; Pascarelli *et al.*, 2006; Labiche *et al.*, 2007; Pasternak *et al.*, 2008; Park *et al.*, 2015; Ping & Coppari, 2016; Coppari *et al.*, 2017; Kantor *et al.*, 2018). Measurements in the DAC remain challenging due to the diamonds detrimentally influencing the signal, *e.g.* their Bragg reflections causing glitches in the spectrum (Abe *et al.*, 2018). While perforated or nano-polycrystalline diamonds are routinely used to minimize such effects (Irifune *et al.*, 2003; Baldini *et al.*, 2011; Ishimatsu *et al.*, 2012), matching material absorption lengths of materials (up to tens of micrometers) along the

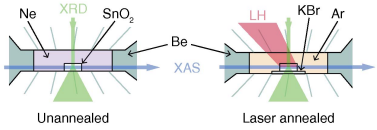

compression axis of the DAC is challenging, and places severe limitations on accessible pressures. Further, high-pressure measurements of any nature become significantly affected by deviatoric stresses once beyond the hydrostatic limit of the system or pressure-transmitting medium (Klotz *et al.*, 2009) due to non-hydrostatic compression arising from the uniaxial nature of the DAC. The use of thermal annealing by focused lasers to relieve such stresses – especially following structural transitions – is commonplace in high-pressure experiments (Salamat *et al.*, 2014), but has yet to become routinely implemented alongside EXAFS measurements. Numerous studies employ near-IR lasers (∼1 µm) to anneal or heat metallic samples at high pressures (Marini *et al.*, 2013; Boccato *et al.*, 2017; Morard *et al.*, 2018), with the advantage that these laser wavelengths can pass through nano-polycrystalline diamonds (Durkee *et al.*, 2019), but these studies typically focus on the XANES component of the XAS spectrum, or do not show fitted EXAFS data, and are focused on single-element systems.

Two recent studies document EXAFS spectra of compounds at high pressure following laser heating – that of Dewaele *et al.* (2016) showing formation of Xe_2O_5 at 82 GPa (near-IR laser, ∼1 µm), and that of Kearney *et al.* (2018) confirming the high-pressure phase of Sn_3N_4 at 105 GPa (CO_2 laser, 10.6 µm). These studies highlight the practicality of EXAFS for determining coordination shells in compounds, complementing diffraction to form a powerful tool for characterizing high-pressure phases and newly synthesized stoichiometries. However, inferring significant information from EXAFS on compounds under extreme pressure is made possible only with high-quality data. The necessity for developing practices for attaining high-quality data on non-metallic compounds at high pressures in a DAC is thus clear. In this article, we describe one such practice: employing *in situ* CO_2 laser heating to thermally anneal SnO_2 into its high-pressure cubic phase, and exploring the inherent disorder in its anion sublattice *via* EXAFS measurements in the radial geometry.

Tin (IV) oxide, SnO_2, is naturally found in the rutile (TiO_2; $P4_2/mnm$) structure as the mineral cassiterite. It is a semiconductor with a band gap of 3.6 eV, with applications in photovoltaics and touchscreen technologies as a transparent conducting oxide (Kílíç & Zunger, 2002), as well as a gas-sensing material (Batzill & Diebold, 2005). A significant pressure-mediated band gap opening has been predicted for its rutile structure, and a number of stable high-density phases (Robertson, 1979; Akgul *et al.*, 2013; Cai *et al.*, 2013), and a similar response has been observed in tin (IV) nitride (Kearney *et al.*, 2018).

The far lighter O atoms in SnO_2 are more susceptible to displacement within the lattice – influenced by such factors as thermal motion, anisotropic strain or grain boundaries – than the heavier Sn. Observations of O sublattice disordering in SnO_2 *via* Raman spectroscopy have recently been reported under quasi-hydrostatic compression up to 20 GPa (Girão *et al.*, 2017, 2018), which is not seen in (XRD) studies (Haines & Léger, 1997). Prior studies on sublattice disordering have focused on rutile ($P4_2/mnm$) SnO_2, as its Raman spectrum is very well understood (Merle *et al.*, 1980; Girão *et al.*, 2017, 2018). Here, we choose to study the high-pressure cubic ($Pa\bar{3}$) phase of SnO_2, stable between ∼20 GPa and 50 GPa (Haines & Léger, 1997). $Pa\bar{3}$ SnO_2 has cations occupying the 4a Wyckoff positions (0, 0, 0), and anions occupying the 8c general positions (u, u, u). The pyrite (FeS_2) structure is obtained when u = 0.38, while at u = 0.25 the Sn coordination polyhedra become cubic and the fluorite (CaF_2; $Fm\bar{3}m$) structure is obtained. Cubic SnO_2 has u = 0.346, appearing as a distorted pyrite structure with its coordination octahedra rotated ∼3.4° relative to ideal pyrite, and a parallel has been made (Girão *et al.*, 2018) with high-pressure cubic PdF_2 (u = 0.3431 (Tressaud *et al.*, 1981). The high symmetry, single Sn coordination and comparatively short unit-cell parameter of this structure allow an EXAFS model with sufficiently few parameters to reliably probe anion disorder.

2. Methods and measurements

Samples of dry SnO_2 (Sigma Aldrich, 99.9%) were loaded in DACs of custom design, equipped with Boehler-Almax design diamond anvils with 300 µm culets. Be was employed as a gasket material, and was initially indented to a thickness of 30 µm and a sample chamber formed by laser micromachining (Hrubiak *et al.*, 2015). Powdered SnO_2 was compressed to form a dense pellet, 25 µm thick and 50 µm wide – matching approximately the calculated absorption length of SnO_2 in its ambient rutile phase (51.1 µm), determined using the Elam database (Elam *et al.*, 2002) and full X-ray cross sections built into the Hephaestus software package (Ravel & Newville, 2005). Two sample geometries were used (Fig. 1): samples were placed in a sample chamber and surrounded by a quasi-hydrostatic pressure-transmitting medium (PTM) of Ne for room-temperature compression without laser heating, or placed on a thin (∼1 µm) window of KBr and surrounded by a PTM of Ar (Smith *et al.*, 2018*a*). In the latter, the KBr window thermally isolates the sample material from the diamond anvil to facilitate efficient laser heating (Salamat *et al.*, 2014). Pressure is determined from the unit-cell volume of the Ne pressure transmitter in room-temperature compression (Dewaele *et al.*, 2008), or the KBr

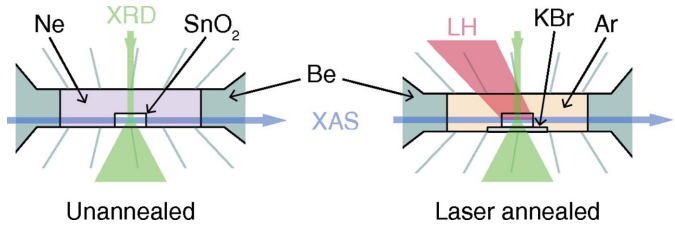

Figure 1
Schematic showing the arrangement of a 50 µm SnO_2 pellet within the diamond anvil cell. XRD is collected axially through the diamonds, while the use of Be as a gasket material permits radial XAS measurements. Left: the sample is placed directly onto the diamond anvil and loaded in a Ne PTM for room-temperature compression. Right: the sample is thermally isolated (Salamat *et al.*, 2014) from the diamond by a thin KBr window, and loaded in Ar for laser-heating experiments.

thermal isolator in laser heating experiments (Dewaele *et al.*, 2012). In both cases, the Be gasket material permits XAS measurements in a radial geometry (Fig. 1) (Park *et al.*, 2015).

CO_2 laser heating was performed at the 16-ID-B beamline of HPCAT (Advanced Photon Source, Argonne National Laboratory, IL, USA) with *in situ* XRD in the axial geometry (Fig. 1) tracking structural changes, and optical pyrometry recording temperatures (Smith *et al.*, 2018*b*). 10.6 µm radiation from the CO_2 laser is focused to a ∼50 µm spot, allowing localized heating of the sample without heating the Be gasket material – which may then soften and deform, or produce mobile and hazardous chemical species. Additionally, Be is highly reflective in the mid-infrared, further facilitating safe use of the laser to anneal sample materials. It should be noted that nano-polycrystalline diamonds feature strong absorption in the mid-IR, negating the use of focused CO_2 lasers to directly heat samples. Further to this, the SnO_2 sample material would not strongly absorb near-IR radiation, instead requiring a metallic coupler to transfer heat to the sample. In this case, the heating is highly non-uniform, and difficulties would arise with matching the absorption length of the sample due to the extraneous material mixed in. Optical pyrometry was used to measure temperature from laser-heated samples, with thermal emission measured from a 7.5 µm region, aligned and comparable in size with the X-ray spot.

On compression in Ne, XRD shows significant phase coexistence [Fig. 2(*a*)], with the lower-pressure orthorhombic ($CaCl_2$-type; *Pnnm*) structure remaining present up to 55 GPa, well beyond its thermodynamic stability region (El Haj Hassan *et al.*, 2013). Despite the quasi-hydrostaticity of the Ne PTM (Klotz *et al.*, 2009), the coexistence of the two competing phases along with anisotropic strain significantly broadens Bragg peaks.

In our laser annealing run, on compression in Ar, we generate pure cubic $Pa\bar{3}$ SnO_2 at 17.5 GPa [Fig. 2(*b*); black line] by CO_2 laser annealing. Though the temperatures were sufficient to surpass the kinetic barrier separating the lower-pressure $CaCl_2$ structure and $Pa\bar{3}$, they were below the detection limit of the optical pyrometry system, which we estimate as 1000 K. On laser annealing at 51 GPa, we observe a further transition away from $Pa\bar{3}$ – we therefore define the phase stability of cubic SnO_2 as 17.5–51 GPa. The necessity of laser annealing for the proper preparation of samples at extreme compression can be seen by the drastic increase in Bragg peak widths when compressing this $Pa\bar{3}$ SnO_2 sample to 32 GPa – with the (1 1 1) peak broadening by 22%, the (3 3 1) by 34%, and the (4 0 2)/(4 2 0) by 54%, as a result of non-hydrostatic compression alone. Similarly, in room-temperature compression in Ne, the FWHM of the (1 1 1) peak is 3.6× greater than when laser annealed in Ar, at equivalent pressures [Fig. 2(*a*)]. Above 40 GPa, we anneal with different temperatures [Fig. 2(*b*)]. Annealing to 1556 ± 20 K gives well defined Bragg peaks. However, the high-**q** reflections are still somewhat broad. Annealing further to 2648 ± 41 K, we see a 15% reduction in the (1 1 1) Bragg peak width, as well as a 35% and 34% reduction of the (3 3 1) and (4 0 2)/(4 2 0) peak widths, respectively. Fig. 2(*c*) shows Rietveld refinement of SnO_2 within the cubic phase only [a = 4.8421 (5) Å and u = 0.3343 (5)], confirming the overcoming of kinetic barriers between phases and the relief of anisotropic strains, *i.e.* the proper preparation of the thermodynamically stable structure at this pressure condition.

Elevated temperatures can lead to the formation of vacancies *via* thermal diffusion, and eventual chemical decomposition. It is thus important to confirm the absence of such vacancies to constrain coordination number parameters in the consequent EXAFS fit. Site vacancies in SnO_2 can lead

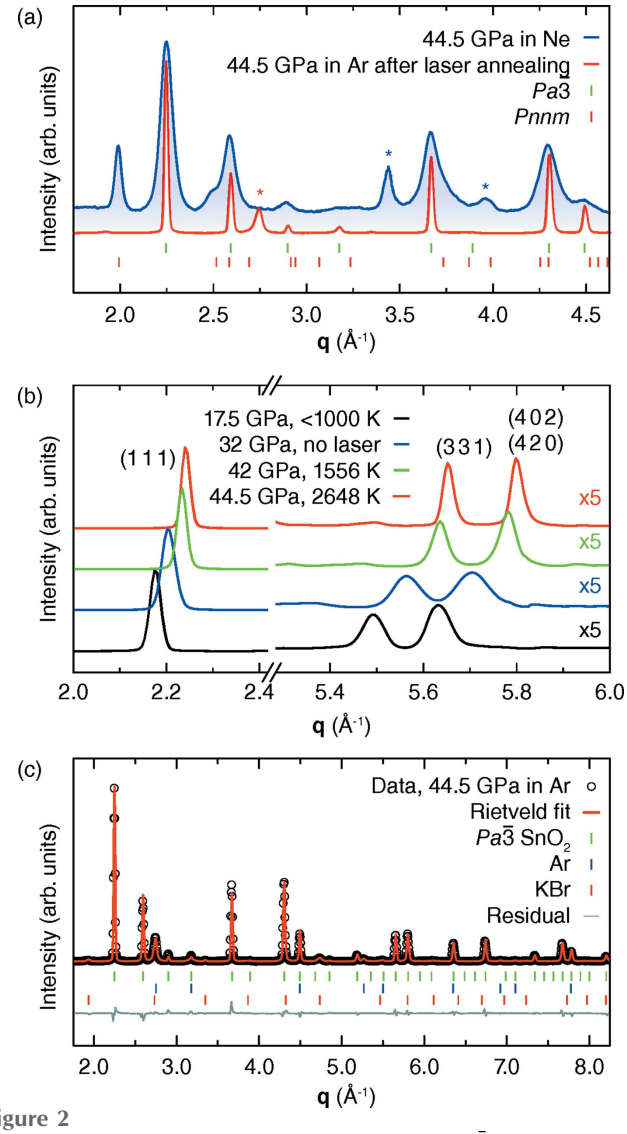

Figure 2
XRD of SnO_2 under pressure. (*a*) (Blue) Cubic ($Pa\bar{3}$, green ticks) and orthorhombic (*Pnnm*, red ticks) phases of SnO_2 coexisting on room-temperature compression in quasi-hydrostatic Ne at 44.5 GPa, well within the stability region of the $Pa\bar{3}$ phase. (Red) $Pa\bar{3}$ SnO_2 following laser heating to 2648 ± 41 K, with no remnants of the *Pnnm* phase and significantly reduced peak widths. Blue asterisks (*) denote reflections from Ne, and red asterisks those from KBr. (*b*) Pressure evolution of select Bragg reflections from $Pa\bar{3}$ SnO_2 from its formation at 17.5 GPa. The effect of thermal annealing is evident in the sharpening of peaks, particularly at high-**q**. Each pattern was collected at 300 K, the legend denotes pressure condition and annealing temperature. (*c*) Rietveld refinement of laser-annealed $Pa\bar{3}$ SnO_2 at 44.5 GPa at room temperature (R_P = 1.177%, R_{WP} = 2.89%).

to intensified fluorescence, whereas we observe only a sharpening of Raman peaks associated with increased crystalline order, and a lowering of background signal. Additionally, no generation of the O_2 vibrational mode was present in Raman spectra following laser heating, XRD shows no evidence of elemental Sn (Salamat *et al.*, 2013), and any attempts to refine site occupancies with the Rietveld method results in unrealistic stoichiometries.

Following XRD measurements at 16-ID-B, XAS experiments were performed in the radial geometry on the Sn *K*-edge (29.2 keV) through the near-edge (XANES) and EXAFS regions across a total energy range of 28.8–30.2 keV at the 16-BM-D beamline of HPCAT (Park *et al.*, 2015). This energy range provides sufficient data below the Sn *K*-edge to optimize the pre-edge region for normalization, and a large k range in EXAFS measurements. Fifteen scans across this energy range were taken in both the annealed and unannealed samples for the purpose of data averaging. This consisted of a total time of approximately 1 h per data point. To calibrate the monochromator, a 58 µm-thick Sn foil (EXAFS Materials, Inc.) was used as a standard. EXAFS spectra reflect the marked changes observed by diffraction following laser heating (Fig. 3). In our unannealed sample compressed in Ne, we see that contributions at higher R are removed *via* destructive interference between scattered photoelectrons from the two coexisting structures, while the first maximum in R (corresponding to the first coordination shell) is both amplified and distorted due to convolution of contributions from the two phases. Despite the quasi-hydrostatic compression afforded by the Ne pressure medium (Klotz *et al.*, 2009), the significant kinetic hindrance across this sluggish, first-order phase transition would make the $Pa\bar{3}$ unstudiable *via* EXAFS without thermal annealing – and we expect the same for many other high-pressure structures. Following laser annealing at 2648 ± 41 K, real-space radial features become more prominent at greater distances [Fig. 3(*a*)], and features of the EXAFS signal become more pronounced at higher frequencies [Fig. 3(*b*)]. With those features from higher coordination shells of $Pa\bar{3}$ no longer obscured by the remnant *Pnnm* phase, an EXAFS fit may be performed up to high k and R.

To further exemplify the effects of CO_2 laser annealing, we subject our recorded spectra to a Morlet wavelet transform [Figs. 3(*c*) and 3(*d*)] (Timoshenko & Kuzmin, 2009). This technique creates a two-dimensional map of the transform space, allowing recognition of coordination shells by their scattering amplitudes, and – crucially – highlighting how multiple scattering paths can contribute to the spectrum, aiding in the design of a real-space *FEFF*-based fitting model (Timoshenko *et al.*, 2012). For instance, in Fig. 3(*d*), multiple scattering paths involving the first Sn (bright feature around 11 Å^{-1} and 3 Å) and third O (around 5 Å^{-1} and 3 Å) can be

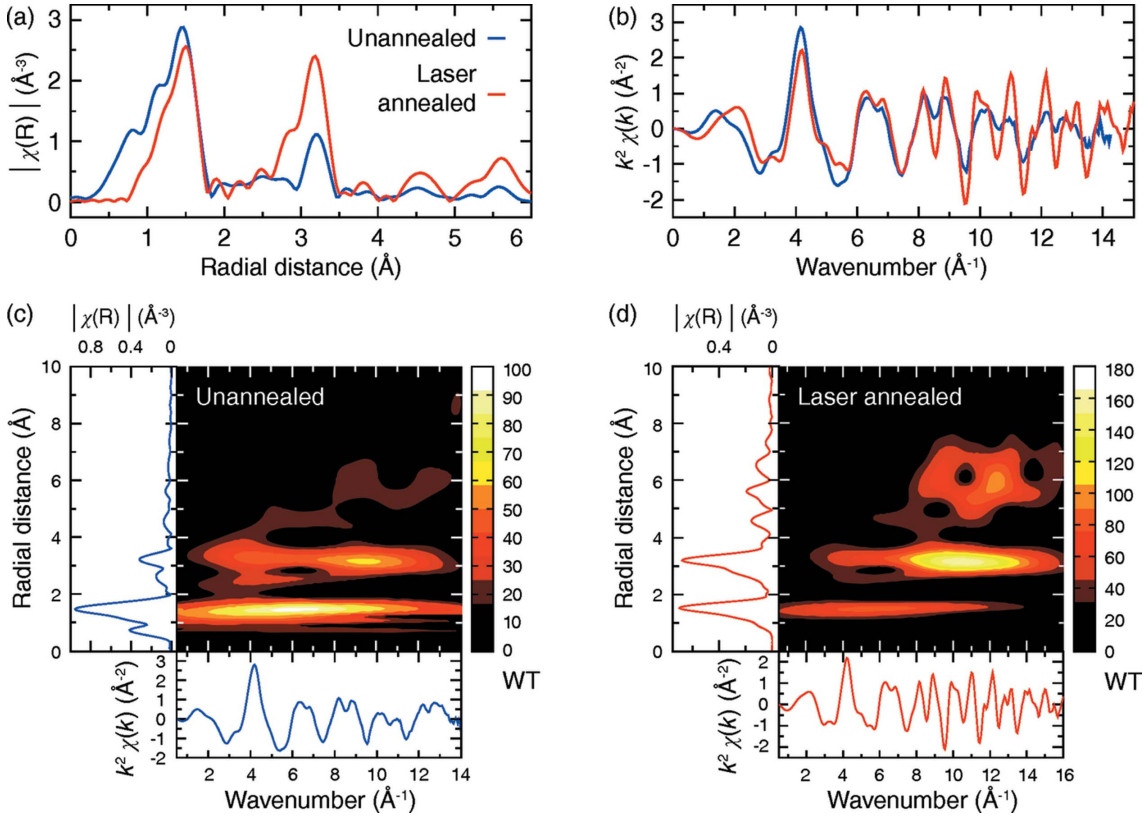

Figure 3
EXAFS signal of SnO_2 at 44.5 GPa, for room-temperature compression (blue) and following laser heating to 2648 ± 41 K (red). (*a*) EXAFS spectrum in k-space. (*b*) Magnitude of the Fourier transform of EXAFS spectra in R-space (without phase correction). (*c*) Morlet wavelet transform for room-temperature compressed sample and (*d*) for the sample following laser annealing.

seen in the visible 'webbing' connecting the two features in transform space. The effects of laser annealing can be best seen in the additional detail in the wavelet transform in Fig. 3(*d*), at higher (*R*, *k*), where those features are obscured and smeared in Fig. 3(*c*) due to aforementioned phase mixing.

3. EXAFS analysis and discussion

XAS data were reduced and analyzed with the DEMETER software package (Ravel & Newville, 2005). EXAFS spectra were fit to calculated scattering potentials generated by FEFF, and fitting was performed with the FEFFIT fitting algorithm within ARTEMIS. The same initial crystallographic coordinates were used for both the EXAFS fit and the Rietveld refinement in Fig. 2(*c*), and an EXAFS fit model was built in a 'bottom up' fashion (Calvin, 2013). Based on diffraction data in Fig. 2 and aforementioned Raman investigations, we model a pure $Pa\bar{3}$ phase free of significant vacancies, *i.e.* the Sn coordination was kept constant during FEFF calculations of the phase term, $\phi(k)$, and the scattering amplitudes, $f(k)$. Partial attenuation due to the Be gasket used in radial geometry gives a passive electron reduction factor, $S_0^2 = 0.87 \pm 0.05$. Initial selection of E_0 was thus performed in ATHENA as the zero crossing of the second derivative of the white line at 29205.45 eV – the short core-hole lifetime of Sn causes significant (10.5 eV) energy broadening, leading to a relatively featureless near-edge structure and, therefore, a relatively featureless second derivative. The absorption spectra of both the SnO_2 sample and the Sn standard were subject to a −7.08 eV correction, accounting for error in the monochromator calibration. The typical selection of the Fermi level of the element as E_0 in FEFF is not always suitable for describing the element in different oxidation states (Bunker, 2010; Calvin, 2013). Pressure-mediated band gap opening in SnO_2 has been predicted (Robertson, 1979; Akgul *et al.*, 2013; Cai *et al.*, 2013), and the same electronic structure change in Sn_3N_4 was described by a shift in effective charge on both the Sn and N species. As such, the term ΔE_0 was used as a fitting parameter to account for both the change in oxidation state of the Sn and further pressure-induced changes in electronic properties. ARTEMIS fits ΔE_0 as 4.58 ± 0.18 eV, within a normal range for EXAFS analysis (Calvin, 2013). It should be noted that ΔE_0 values greater than 2–3 eV can correlate with shifts in coordination shell radii, and that this effect is more prominent for atoms with dominant features in the lower *k* region of the EXAFS spectrum such as O (Fig. 3) (Bunker, 2010). To break this correlation, fitting was performed in *k* powers 1, 2 and 3 simultaneously (Calvin, 2013), and no correlation was observed between the shift in O coordination shells and their distances *R* from the absorbing Sn.

In order to reduce the number of variables in the fitting model, whilst also retaining an accurate description of thermal motion, the correlated Debye model was used to represent disorder with increasing *R*. On an atomic weight argument alone, one expects that the thermal motion along Sn—O paths will be of a higher frequency than that along Sn—Sn. Thus, we model Sn and O shells with individual Debye temperatures, and multiple scattering paths were modeled using combinations of these temperatures, depending on their geometry. Shell displacements for the Sn—Sn and Sn—O shells were treated independently, as was the displacement of each individual shell. Multiple scattering paths were included in the fit model, informed by the Morlet wavelet transform in Figs. 3(*c*) and 3(*d*). Assuming a harmonic potential between two atoms, scattering paths may be modeled with a Gaussian function, and variation about mean atomic positions are described accurately by the Debye–Waller term. However, for SnO_2 we expect disorder at these pressure conditions (Girão *et al.*, 2018), and the Gaussian function is no longer sufficient, meaning that higher moments of the distribution must be considered. Thus, to study disordering, the cumulant expansion of the EXAFS equation was used (Boccato *et al.*, 2016; Ravel *et al.*, 2006),

$$k\chi(k) = \frac{NS_0^2 \exp(-2C_1/\lambda)}{C_1^2} |f(k)| \times \exp\left(-2k^2C_2 + \frac{2}{3}k^4C_4 + \ldots\right) \times \sin\left[2kC_1 - \frac{4}{3}k^3C_3 + \ldots + \phi(k)\right]. \quad (1)$$

Here, the first cumulant, C_1, is the average separation, the second cumulant, C_2, is contained within the Debye–Waller factor and describes the mean square relative displacement (MSRD), while the third and fourth cumulants in the expansion (C_3 and C_4) describe anharmonicity between the absorbing and scattering atoms (Dalba & Fornasini, 1997).

Fig. 4 shows the results of fitting scattering paths of annealed $Pa\bar{3}$ SnO_2 within the fit window 1.0–6.1 Å in *R*- and 1.0–15.9 $Å^{-1}$ in *k*-space. This fitting window gave a total of 50 independent points, as determined by the Nyquist criterion, $N_{ind} = 2\Delta k \Delta R/\pi + 2$. It is common to choose a starting point in momentum space of 2–3 $Å^{-1}$; in this case, we chose a starting point of 1 $Å^{-1}$. This was guided by the wavelet transform showing that the first feature in the EXAFS spectrum is dominated by the Sn–O_{1st} coordination shell, therefore the low *k* region was crucial for properly modeling the first oxygen shell. It can also be seen in the wavelet transform that the multiple scattering path contribution in the momentum space region below 3 $Å^{-1}$ is minimal. We believe that this is due to the large energy broadening induced by the short core-hole lifetime of tin. Of the 50 independent points, 30 fitting parameters were allowed to float, which was necessary to properly describe the independent motion of each coordination shell. The maximum of 6.1 Å was chosen to include statistically significant multiple scattering paths, as both determined by FEFF, and visible in the wavelet transformation. A Hanning window function with a sill of 1.0 $Å^{-1}$ was used to compensate for the finite Fourier transform window. Two important points must be made regarding the fit model: first, the *R*-space fit remains good below 1.0 Å (the start of the fit window) and, second, changing the fitting range had minimal effects on the quality of the fit (affecting parameter values only within their uncertainties), both giving further confidence in the model

Table 1
Atomic distances to 5 Å for $Pa\bar{3}$ SnO_2 at 44.5 GPa from EXAFS and XRD along with parallel and perpendicular anharmonicity components, $\sigma_{\parallel}$ and $\sigma_{\perp}$, and higher cumulant terms.

The 0 values were found to be 0 within the uncertainty of the fit, and therefore reported as 0. Debye temperatures determined from the fit for the Sn—Sn paths and Sn—O paths are Θ_{Sn-Sn} = 384 ± 16 K and Θ_{Sn-O} = 1480 ± 200 K, respectively.

		Distance (Å)						
Path	N	EXAFS	XRD	Difference	$\sigma_{\parallel}^2$ (Å^2)	$\sigma_{\perp}^2$ (Å^2)	C_3 (Å^3)	C_4 (Å^4)
Sn—O_{1st}	6	1.975 (2)	1.977	0.002	0.0017 (2)	0.004 (2)	0	0
Sn—O_{2nd}	2	2.66 (5)	2.78	0.12	0.00201 (26)	0.33 (8)	−0.0022 (6)	0
Sn—O_{3rd}	6	3.32 (2)	3.44	0.12	0.00203 (26)	0.41 (4)	0	0
Sn—Sn_{1st}	12	3.429 (2)	3.424	−0.005	0.0041 (2)	0.017 (4)	0	0
Sn—O_{4th}	6	3.94 (3)	3.95	0.01	0.00201 (26)	0.06 (3)	0.0004 (3)	0
Sn—O_{5th}	12	4.62 (2)	4.41	−0.21	0.00201 (26)	0.93 (4)	0.0007 (4)	0
Sn—O_{6th}	6	4.91 (5)	4.85	−0.06	0.00202 (26)	0.3 (1)	−0.0038 (5)	0.00005 (4)
Sn—Sn_{2nd}	6	4.839 (9)	4.842	0.003	0.0043 (2)	0.02 (1)	0	0

used. Table 1 shows the results of fitting each scattering path to equation (1). Some lengths are measured shorter by EXAFS than XRD, and some longer. The measurement of shorter length by EXAFS is an uncommon, but not unphysical, phenomenon, examples of which typically come from paths with significant atomic weight discrepancies, such as Sr–O and Sr–P in strontium compounds (O'Day *et al.*, 2000), As–O in meta-zeunerite (Hennig *et al.*, 2001), and *L*–Co (*L* = La or Pr) in lanthanide cobaltites (Pandey *et al.*, 2006).

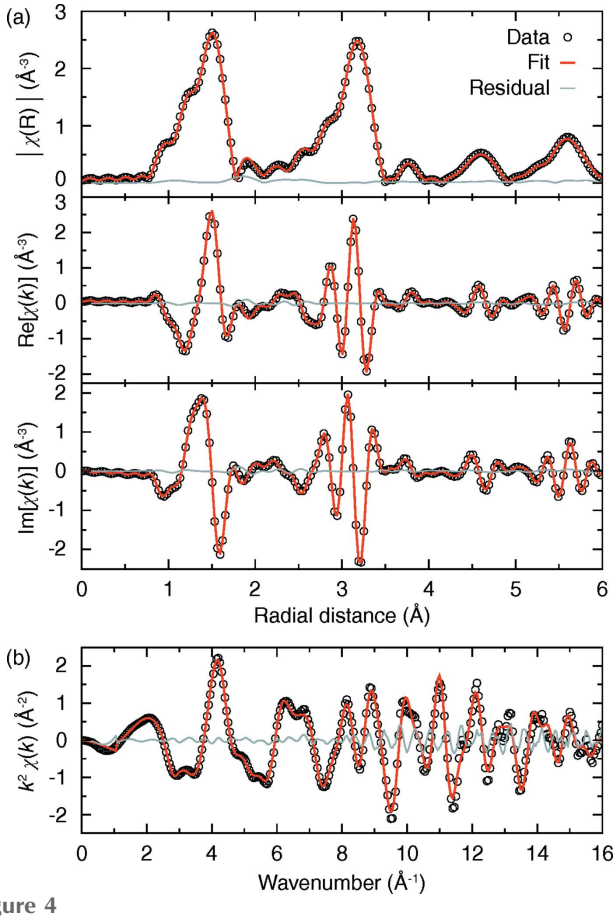

Figure 4
Fitting of EXAFS spectrum to calculated scattering potentials for each significant path up to 6 Å, displayed in (*a*) radial space (without phase correction) and (*b*) momentum space (R = 0.0018, 0.0015, 0.0019 for k-weight 1, 2, 3, respectively). All displayed spectra are weighted by k^2.

The good agreement between EXAFS and XRD regarding Sn—Sn distances provides further confidence in the fit model used. Meanwhile, the distribution of Sn—O distances measured on the unit-cell scale (*via* EXAFS) relative to those measured by XRD is consistent with predicted disordering of the O sublattice under pressure (Girão *et al.*, 2018).

The third cumulant, C_3, in equation (1) is correlated with the phase shift term, and can be used to describe radial distributions exhibiting asymmetry that might shift its mean from the ideal position (*i.e* that if it were purely Gaussian). Positive C_3 shifts the distribution to lower R, and negative C_3 to higher R. Notably, in Table 1, the sign and magnitude of C_3 is not correlated with the difference in distances measured by EXAFS and XRD. Both Sn—O_{2nd} and Sn—O_{6th} have negative C_3, indicating asymmetric distributions whose outer (higher R) tails are emphasized, while the Sn—O_{4th} and Sn—O_{5th} shells are weighted to lower R. The 4th cumulant, C_4, is correlated with the amplitude reduction term and the second cumulant, or the MSRD, $\sigma_{\parallel}^2$. The non-zero C_4 for the Sn—O_{6th} path likely arises from its higher MSRD, creating an outlier in its distribution which cannot be accounted for by the correlated Debye model.

The Rietveld refinement in Fig. 2(*c*) is constrained to the symmetry and atomic positions described earlier, imposing that each Sn sits at the center of an octahedron of six O atoms. Meanwhile, EXAFS allows the determination of distances to each of the atomic coordination shells within the local environment of the Sn atoms, and, with the employment of laser annealing to relax the system into a pure $Pa\bar{3}$ structure with deviatoric stresses minimized, data quality remains good to the highest region of k-space, and path lengths up to the farthest distance in a single unit cell (∼5 Å) can be fitted with confidence. From Table 1, it can be seen that shells composed of O atoms deviate substantially from their positions imposed by symmetry, with no appearent trend, implying significant anisotropy in the Sn—O shells and disordering of the O sublattice. It should be noted that any uncertainties that may arise from a large ΔE_0 could not explain the large disorder apparent in the O positions, especially considering the highly ordered Sn positions. Thus, we analyze the level of disorder using the techniques set forth by Fornasini *et al.* (2001) and Boccato *et al.* (2016).

The Fourier transform of the EXAFS signal gives a one-dimensional projection of the three-dimensional distributions of each atomic shell. From this, the MSRD of a shell describes its displacement parallel to the path connecting it to the absorbing atom, $\sigma_{\parallel}^2$, to a first-order approximation, and is derived directly from the fit. For a full understanding of anisotropies in the motion of the atoms, one can also consider the perpendicular displacement of each shell, $\sigma_{\perp}^2$, derived by comparison of the instantaneous relative atomic distances, $\langle r \rangle$, measured by EXAFS (given by $\langle |\bar{r_a} - \bar{r_b}| \rangle$, where a is the absorbing and b the scattering atom) and the average atomic separations, R, provided by XRD (given by $|\langle \bar{r_a} \rangle - \langle \bar{r_b} \rangle|$), through $\langle \sigma_{\perp}^2 \rangle \simeq R(\langle r \rangle - R)$ (Fornasini *et al.*, 2001; Fornasini & Grisenti, 2015; Boccato *et al.*, 2016).

Both $\sigma_{\parallel}^2$ and $\sigma_{\perp}^2$ for laser-annealed cubic SnO_2 at 44.5 GPa are reported in Table 1. The small deviations between symmetry-constrained distances and those measured by EXAFS for the Sn lattice are mirrored in the low $\sigma_{\perp}$ for Sn—Sn coordination shells. Meanwhile, perpendicular disorder for Sn—O coordination shells varies greatly, further evidencing sublattice disordering as measured for rutile SnO_2 (Girão *et al.*, 2017, 2018). The second Sn—O shell contains two O atoms, contributing to what has been described as a '6+2' coordination for $Pa\bar{3}$ SnO_2 (Haines & Léger, 1997), and shows significant disordering. While the scattering potential is comparatively low for this shell – one result being that it features the greatest percentage uncertainty of all shells included – we find that its inclusion vastly improves the fit, consistent with the '6+2'-coordinated Sn description set forth by Haines & Léger (1997). On testing the stability of the fit model (*e.g.* by altering the fitting window), the Sn—O_{2nd} shell is the only shell whose variation exceeds its uncertainty – likely due again to its low scattering potential owing to having only two O atoms. Each of these two O atoms within the Sn—O_{2nd} shell form one-sixth of the octahedra surrounding the nearest Sn atoms, and as such their positions are highly correlated with those of the O in the nearest-neighbor octahedron. It is therefore unsurprising that this shell is most sensitive to disordering, slight tilting of the corner-linked SnO_6 octahedra move these O atoms significantly with respect to the absorbing Sn. The large $\sigma_{\perp}$ values equate to increased eccentricity of the 'thermal ellipsoids' occupied by O atoms, and the same effect with pressure has been observed in CdTe (Fornasini *et al.*, 2018).

4. Conclusion

Combinational approaches using XRD and EXAFS can provide more complete structural insight into compounds with large mass differences between constituent elements. We have applied this to the DAC, and propose a protocol for quantitative analysis of structural and thermal disorder in compounds under extreme compression. Central to this approach is the use of CO_2 laser annealing to produce a phase-pure sample with relieved strain. We find that cubic SnO_2 at 44.5 GPa, despite displaying high amounts of cation order *via* both XRD and EXAFS, exhibits anion disorder seen with EXAFS – shown by the high level of anisotropy in its coordination shells. This is assigned to the higher mobility of the lighter O anions within the lattice when compared with the Sn cations, the latter remaining on their crystallographic lattice positions while the former are non-periodically displaced (Table 1).

We thus confirm thermally annealed, high-pressure EXAFS as a powerful method for quantifying atomic disordering, overcoming some of the prior difficulties associated with EXAFS analysis under extreme conditions. Notably, the employment of thermal annealing relaxes sample into states which are suitable for working with computationally derived standards such as those produced by crystal structure prediction softwares. This is a crucial factor for EXAFS measurements and analyses of structures which exist only under extreme conditions, *e.g* the Xe oxides reported by Dewaele *et al.* (2016), where appropriate physical reference materials may not exist. We propose this technique as a necessary development for further analysis of anion disordering recently observed in compounds such as SnO_2 (Girão *et al.*, 2018), as well as for confirming structures of compounds at high pressures (Kearney *et al.*, 2018).

Acknowledgements

Portions of this work were performed at HPCAT (Sector 16), Advanced Photon Source (APS), Argonne National Laboratory.

Funding information

This research was sponsored in part by the National Nuclear Security Administration under the Stewardship Science Academic Alliances program through DOE Cooperative Agreement #DE-NA0001982. HPCAT operations are supported by DOE-NNSA's Office of Experimental Sciences. The Advanced Photon Source is a US Department of Energy (DOE) Office of Science User Facility operated for the DOE Office of Science by Argonne National Laboratory under Contract No. DE-AC02-06CH11357.

References

Abe, H., Aquilanti, G., Boada, R., Bunker, B., Glatzel, P., Nachtegaal, M. & Pascarelli, S. (2018). *J. Synchrotron Rad.* **25**, 972–980.
Akgul, F. A., Gumus, C., Er, A. O., Farha, A. H., Akgul, G., Ufuktepe, Y. & Liu, Z. (2013). *J. Alloys Compd.* **579**, 50–56.
Aquilanti, G., Crichton, W. A. & Pascarelli, S. (2003). *High Pressure Res.* **23**, 301–305.
Baldini, M., Yang, W., Aquilanti, G., Zhang, L., Ding, Y., Pascarelli, S. & Mao, W. L. (2011). *Phys. Rev. B*, **84**, 014111.
Batzill, M. & Diebold, U. (2005). *Prog. Surf. Sci.* **79**, 47–154.
Boccato, S., Sanson, A., Kantor, I., Mathon, O., Dyadkin, V., Chernyshov, D., Carnera, A. & Pascarelli, S. (2016). *J. Phys. Condens. Matter*, **28**, 355401.
Boccato, S., Torchio, R., Kantor, I., Morard, G., Anzellini, S., Giampaoli, R., Briggs, R., Smareglia, A., Irifune, T. & Pascarelli, S. (2017). *J. Geophys. Res. Solid Earth*, **122**, 9921–9930.
Bunker, G. (2010). *Introduction to XAFS: A Practical Guide to X-ray Absorption Fine Structure Spectroscopy*. Cambridge University Press.

Cai, L. G., Liu, F. M., Zhang, D. & Zhong, W. W. (2013). *Physica B*, **408**, 73–78.
Calvin, S. (2013). *XAFS for Everyone.* Boca Raton: CRC Press.
Coppari, F., Thorn, D. B., Kemp, G. E., Craxton, R. S., Garcia, E. M., Ping, Y., Eggert, J. H. & Schneider, M. B. (2017). *Rev. Sci. Instrum.* **88**, 083907.
Dalba, G. & Fornasini, P. (1997). *J. Synchrotron Rad.* **4**, 243–255.
Dewaele, A., Belonoshko, A. B., Garbarino, G., Occelli, F., Bouvier, P., Hanfland, M. & Mezouar, M. (2012). *Phys. Rev. B*, **85**, 214105.
Dewaele, A., Datchi, F., Loubeyre, P. & Mezouar, M. (2008). *Phys. Rev. B*, **77**, 094106.
Dewaele, A., Worth, N., Pickard, C. J., Needs, R. J., Pascarelli, S., Mathon, O., Mezouar, M. & Irifune, T. (2016). *Nat. Chem.* **8**, 784–790.
Durkee, D., Smith, D., Torchio, R., Petitgirard, S., Briggs, R., Kantor, I., Evans, S. R., Chatterji, T., Irifune, T., Pascarelli, S., Lawler, K. V., Salamat, A. & Kimber, S. A. (2019). *J. Solid State Chem.* **269**, 540–546.
Elam, W., Ravel, B. & Sieber, J. (2002). *Radiat. Phys. Chem.* **63**, 121–128.
El Haj Hassan, F., Moussawi, S., Noun, W., Salameh, C. & Postnikov, A. V. (2013). *Comput. Mater. Sci.* **72**, 86–92.
Fornasini, P. & Grisenti, R. (2015). *J. Synchrotron Rad.* **22**, 1242–1257.
Fornasini, P., Grisenti, R., Irifune, T., Shinmei, T., Mathon, O., Pascarelli, S. & Rosa, A. D. (2018). *J. Phys. Condens. Matter*, **30**, 245402.
Fornasini, P., Monti, F. & Sanson, A. (2001). *J. Synchrotron Rad.* **8**, 1214–1220.
Girão, H. T., Cornier, T., Daniele, S., Debord, R., Caravaca, M. A., Casali, R. A., Mélinon, P. & Machon, D. (2017). *J. Phys. Chem. C*, **121**, 15463–15471.
Girão, H. T., Hermet, P., Masenelli, B., Haines, J., Mélinon, P. & Machon, D. (2018). *Phys. Rev. Lett.* **120**, 265702.
Haines, J. & Léger, J. M. (1997). *Phys. Rev. B*, **55**, 11144–11154.
Hennig, C., Reich, T., Funke, H., Rossberg, A., Rutsch, M. & Bernhard, G. (2001). *J. Synchrotron Rad.* **8**, 695–697.
Hrubiak, R., Sinogeikin, S., Rod, E. & Shen, G. (2015). *Rev. Sci. Instrum.* **86**, 072202.
Irifune, T., Kurio, A., Sakamoto, S., Inoue, T. & Sumiya, H. (2003). *Nature*, **421**, 599–600.
Ishimatsu, N., Matsumoto, K., Maruyama, H., Kawamura, N., Mizumaki, M., Sumiya, H. & Irifune, T. (2012). *J. Synchrotron Rad.* **19**, 768–772.
Kantor, I., Marini, C., Mathon, O. & Pascarelli, S. (2018). *Rev. Sci. Instrum.* **89**, 013111.
Kearney, J. S. C., Graužinytė, M., Smith, D., Sneed, D., Childs, C., Hinton, J., Park, C., Smith, J. S., Kim, E., Fitch, S. D. S., Hector, A. L., Pickard, C. J., Flores-Livas, J. A. & Salamat, A. (2018). *Angew. Chem. Int. Ed.* **57**, 11623–11628.
Kílíç, C. & Zunger, A. (2002). *Phys. Rev. Lett.* **88**, 095501.
Klotz, S., Chervin, J.-C., Munsch, P. & Le Marchand, G. (2009). *J. Phys. D Appl. Phys.* **42**, 075413.
Labiche, J. C., Mathon, O., Pascarelli, S., Newton, M. A., Ferre, G. G., Curfs, C., Vaughan, G., Homs, A. & Carreiras, D. F. (2007). *Rev. Sci. Instrum.* **78**, 091301.
Marini, C., Kantor, I., Mathon, O. & Pascarelli, S. (2013). *High. Press. Res.* **33**, 108–113.
Merle, P., Pascual, J., Camassel, J. & Mathieu, H. (1980). *Phys. Rev. B*, **21**, 1617–1626.
Morard, G., Boccato, S., Rosa, A. D., Anzellini, S., Miozzi, F., Henry, L., Garbarino, G., Mezouar, M., Harmand, M., Guyot, F., Boulard, E., Kantor, I., Irifune, T. & Torchio, R. (2018). *Geophys. Res. Lett.* **45**, 11074–11082.
O'Day, P. A., Newville, M., Neuhoff, P. S., Sahai, N. & Carroll, S. A. (2000). *J. Colloid Interface Sci.* **222**, 184–197.
Pandey, S. K., Khalid, S., Lalla, N. P. & Pimpale, A. V. (2006). *J. Phys. Condens. Matter*, **18**, 10617–10630.
Park, C., Popov, D., Ikuta, D., Lin, C., Kenney-Benson, C., Rod, E., Bommannavar, A. & Shen, G. (2015). *Rev. Sci. Instrum.* **86**, 072205.
Pascarelli, S., Mathon, O., Muñoz, M., Mairs, T. & Susini, J. (2006). *J. Synchrotron Rad.* **13**, 351–358.
Pasternak, S., Aquilanti, G., Pascarelli, S., Poloni, R., Canny, B., Coulet, M. V. & Zhang, L. (2008). *Rev. Sci. Instrum.* **79**, 085103.
Ping, Y. & Coppari, F. (2016). *High. Press. Res.* **36**, 303–314.
Ravel, B., Kim, Y. I., Woodward, P. M. & Fang, C. M. (2006). *Phys. Rev. B*, **73**, 184121.
Ravel, B. & Newville, M. (2005). *J. Synchrotron Rad.* **12**, 537–541.
Robertson, J. (1979). *J. Phys. Solid State Phys.* **12**, 4767.
Salamat, A., Briggs, R., Bouvier, P., Petitgirard, S., Dewaele, A., Cutler, M. E., Corà, F., Daisenberger, D., Garbarino, G. & McMillan, P. F. (2013). *Phys. Rev. B*, **88**, 104104.
Salamat, A., Fischer, R. A., Briggs, R., McMahon, M. I. & Petitgirard, S. (2014). *Coord. Chem. Rev.* **277–278**, 15–30.
Smith, D., Shelton, D. P., Ellison, P. B. & Salamat, A. (2018*a*). *Rev. Sci. Instrum.* **89**, 103902.
Smith, D., Smith, J. S., Childs, C., Rod, E., Hrubiak, R., Shen, G. & Salamat, A. (2018*b*). *Rev. Sci. Instrum.* **89**, 083901.
Timoshenko, J. & Kuzmin, A. (2009). *Comput. Phys. Commun.* **180**, 920–925.
Timoshenko, J., Kuzmin, A. & Purans, J. (2012). *Comput. Phys. Commun.* **183**, 1237–1245.
Tressaud, A., Soubeyroux, J., Touhara, H., Demazeau, G. & Langlais, F. (1981). *Mater. Res. Bull.* **16**, 207–214.